

# 2D image head pose estimation via latent space regression under occlusion settings

José Celestino, Manuel Marques, Jacinto C. Nascimento, João Paulo Costeira

*Institute for Systems and Robotics, Instituto Superior Técnico, Lisboa, Portugal*

---

## Abstract

Head orientation is a challenging Computer Vision problem that has been extensively researched having a wide variety of applications. However, current state-of-the-art systems still underperform in the presence of occlusions and are unreliable for many task applications in such scenarios. This work proposes a novel deep learning approach for the problem of head pose estimation under occlusions. The strategy is based on latent space regression as a fundamental key to better structure the problem for occluded scenarios. Our model surpasses several state-of-the-art methodologies for occluded HPE, and achieves similar accuracy for non-occluded scenarios. We demonstrate the usefulness of the proposed approach with: (i) two synthetically occluded versions of the BIWI and AFLW2000 datasets, (ii) real-life occlusions of the Pandora dataset, and (iii) a real-life application to human-robot interaction scenarios where face occlusions often occur. Specifically, the autonomous feeding from a robotic arm.

*Key words:* Head pose estimation, Occlusion, Latent space, Euler angles

---

## 1. Introduction

Extensively researched over the last 25 years [1, 2], 2D head pose estimation (HPE) is a challenging but compelling and relevant computer vision

---

*Email addresses:* Corresponding author - jose.celestino@tecnico.ulisboa.pt (José Celestino), manuel@isr.tecnico.ulisboa.pt (Manuel Marques), jan@isr.tecnico.ulisboa.pt (Jacinto C. Nascimento), jpc@isr.tecnico.ulisboa.pt (João Paulo Costeira)

problem, since several applications benefit from knowing the position of the head. This includes driving safety systems [3, 4], motion capture [5], human behavior analysis in smart rooms to monitor activities [6], human interaction in meeting and workplaces [7, 8], surveillance and safety [9] and target advertisement [10]. Succinctly, this problem consists in approximately determining the orientation of a head in a 2D image.

Deep learning has become a fundamental tool to address this problem reaching state-of-the-art (SoTA) performances. However, current deep learning based systems scarcely approach the HPE under the facial occlusions. This is a fundamental challenge that must be somewhat addressed, since occlusions emerge from numerous applications (*e.g.* see Fig. 1). As it will be addressed herein, a focus is given to scenarios where occlusions are typical and abundant, an issue that is seldom in most recent HPE approaches.

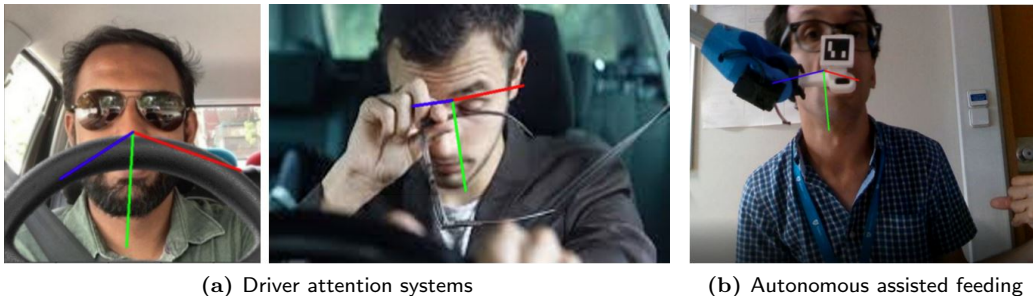


Figure 1: Head pose problem for occlusion scenarios (blue axis points towards estimated face direction).

To address the above challenge we present a novel deep learning methodology based on latent space regression that enables to tackle the problem of head occlusions. As per the hierarchical representation of HPE techniques and applications defined in [2], our work is aligned with a CNN-based training method which has applications for problems that involve 2D images of low or high resolution, such as driver attention [3], surveillance [9] and face frontalization [11].

Our purpose is twofold. Particularly, we aim (i) to achieve robust 2D head pose estimation for occluded faces, and (ii) to extend on current works that achieve SoTA estimation results in non-occluded benchmark datasets.

The contributions can be highlighted as follows<sup>1</sup>:

- A theoretical learning framework for HPE relying on latent space regression with multi-loss.
- An ablation study reporting how the above innovation impacts on the HPE estimates.
- Achievement of SoTA accuracy results for HPE in several benchmark datasets with occlusions. As a side result we also demonstrate the effectiveness of the proposed approach which surpasses SoTA in scenarios without occlusion.
- A new application for HPE. Specifically, the ability to feed disabled people using a robotic arm.
- A simple auxiliary approach, yet effective, to generate synthetic occlusions. In this way, it is possible to build new (occluded) datasets with any desired occlusion object.

## 2. Related work

In this section we describe human head pose estimation related literature regarding model based and learning based approaches.

### 2.1. Model-based strategies

Model-based methods aim to recover the head motion from one (or more) camera views using a, *e.g.*, 2D rigid model. Such a model is usually parameterized with a kinematic chain and thereby the pose is represented by a vector of landmarks (*i.e.*, points) and the corresponding joint angles. The goal is to fit the model to observations (*i.e.*, features) collected from the image.

The authors from [12] propose a method that performs face landmark and keypoint prediction. Landmarks represent a specific set face points (*e.g.*, eyes, nose) that define a rigid model. Keypoints are feature head points extracted and tracked throughout frames. The number of keypoints per frame is not fixed as in the facial landmarks, since it depends on how many are

---

<sup>1</sup>Code available at <http://github.com/Jose-Celestino/OcclusionHPE>

tracked between two frames. They also do not have fixed locations. The authors use the Features from Accelerated Segment Test (FAST) and a pyramidal Lucas-Kanade feature tracker to detect and track these keypoints. They use a Kalman filter to blend both keypoint (prediction step) and landmark detection (correction step). This fusion method shows better results than either using only keypoints or landmarks.

In [13] the authors propose a geometry-based method capable of estimating the head pose from a single 2D face image which only requires four non-coplanar 2D feature points. The idea of using less feature points is to reduce computational complexity. They perform feature point normalization and a 3D morphing method with spherical parametrization to adapt the 3D facial model to each individual and counter generalization issues.

The idea in [14] is to implement a model that maps an input image to a 3D FLAME head mesh representation and simultaneously learns the head pose, shape, and expression. The training methodology is landmark-based via optimization of two loss components, a reprojection loss and a shape plus expression loss. The first one is based on the full head dense 2D landmarks and aims to assess the pose accuracy, while the second measures how well the predicted 3D head mesh fits. The authors also developed a dataset of nearly 45k images to train and validate the model, but only 16% of them include occlusions.

The work developed in [15] approaches the 3D face alignment and pose estimation problems as a 3D Morphable Model (3DMM) parameter regression problem. Their strategy aims to regress the rotation matrix and translation vector to estimate the pose in order to avoid the ambiguity caused by the gimbal lock problem that occurs when faces get close to profile view. The authors use a fast lightweight backbone convolutional neural network and apply both a landmark regressor and a cost function with two terms, the weighted parameter distance cost (WPDC) and the vertex distance cost (VDC). This cost function minimizes the vertex distances between a fitted 3D face and the ground truth. They also establish a 3D aided short-video-synthesis method which helps to achieve smoother estimation results in videos.

Occlusion has also been addressed in the problem of HPE, aided by model-based approaches. The authors in [16] estimate the head pose of partially occluded faces by tracking the displacement of a face feature with respect to the center of the head. They use CamShift to track the center of the head and a iterative Lucas-Kanade optical flow tracker to track the feature face point. This method has disadvantages, since it requires the mouth not to be

occluded and also it relies on discontinued software and hardware.

The authors of [17] focus on achieving robust facial landmark detection for severe occlusions and images with large head poses. They use landmark visibility probabilities to measure if a landmark is visible, and perform occlusion prediction. They add a prior occlusion pattern loss to aid the performance of the prediction. This work, however, does not have real-time tracking capabilities and does not specifically focus on estimating poses.

The method of [18] estimates facial landmark locations, head pose and facial deformation under facial occlusions. This procedure updates each estimation parameter based on the previously estimated values of the others. According to the authors, the combined framework achieves better results in head pose estimation than other methods that use all landmarks (as a rigid model) instead of only the ones that are visible. However, this work only evaluates yaw angles.

## *2.2. Learning-based strategies*

As mentioned by the authors of [19], model-based methods rely on the chosen head model and are sensitive to errors in landmark/keypoint detection. Learning-based HPE approaches have been proposed to avoid these drawbacks. The idea behind such strategies is to directly estimate the pose from image inputs to neural networks. These networks are commonly trained through regression of Euler angles or rotation matrix parameters using head pose datasets with ground-truth pose annotations.

The authors from [19] propose a deep learning strategy which employs a backbone neural network augmented with three fully-connected layers, each one used to predict a different Euler angle. The authors follow a multi-loss approach that combines a classification loss with a weighted regression loss for each angle. Cross-entropy and a mean squared error losses are used for the classification and regression, respectively. The classification component aids the model to predict the vicinity of the pose and the regression component helps it to achieve fine-grained estimation. This multi-loss approach has inspired other authors for the HPE problem [1, 20].

Another solution, FSA-Net [21], applies the soft-stage wise regression problem defined in [22] to solve the HPE challenge. Feature maps from input images are extracted and fused together across several stages. Each stage outputs probabilities distributions for the angle interval classes and refines the estimation within an angle interval assigned by the previous stage. The

estimated pose is given by the soft-stage regression function, which corresponds to the sum of the product between probability distribution and the values of pose groups at each stage.

The method *img2pose* presented in [23] proposes a novel real-time capable solution to simultaneously perform face detection and head pose estimation with 6 degrees of freedom (Euler rotation and 3D translation vectors) in an image without requiring a prior face detection step. This estimation is computationally less costly than the one of model-based approaches which regress  $6 \times 2D = 136$  elements, instead of only 6. Moreover, this pose allows to align the 3D face with its location in an image, which eliminates the need for face detectors.

The authors of [1] extend the multi-loss approach of Hopenet [19] for full  $360^\circ$  yaw estimation. They generate a new dataset with full range of yaws by combining 300W-LP with computed Euler angle data from the CMU Panoptic Dataset. They use binary-cross entropy as for the classification loss and introduce a new wrapped loss for the regression component. They also utilize a lighter backbone network to facilitate real-time applications. The modifications made to Hopenet achieved SoTA of performance for full-range head pose estimation.

In [24], a quaternion-based multi-regression loss method (QuatNet) is proposed. The model is trained exclusively with RGB images. The loss combines L2 regression loss for precise angle prediction and ordinal regression loss to learn robust features that rank different intervals of angles. This allows to address the non-stationary property in head pose estimation, where pose variations within each angle interval is different.

The ambiguity problem of rotation labels is addressed in [25]. They propose a landmark-free method (6DrepNet) that uses rotation matrix representation and a geodesic loss for efficient and robust head pose regression. Besides removing ambiguity problems, the authors claim it avoids performance stabilizing measures such as the discretization of the rotation variables into classification problems.

The authors from [26] claim that landmark-free methods disregard the perspective distortion in face images, caused by the misalignment of the face with the camera coordinate system. They propose an image rectification method to reduce this effect and to achieve higher HPE accuracy with a lightweight network. However, this method involves a face detection step and does not take into account the impact of occlusions when rectifying a head image.

### 2.3. Relations with SoTA methodologies

In this section we define and fit our methodology within the hierarchical representations for HPE methods presented in the extensive survey of [2]. We therefore frame our technique according to the following core aspects:

- **Head pose representation** - In this work, we focus on estimating the rotations that define the head pose. There are diverse ways of representing these rotations, in particular, with (i) *quaternions* [27], with rotation matrices [25, 28], or with (ii) *Euler angles* [1, 19, 21]. Our technique represents head pose according to *Euler angles* ( $\alpha, \beta, \gamma$  - yaw, pitch and roll), which can be visually interpreted.
- **Type of input data** - The training and testing datasets depend on the type of input data used. HPE can be performed in three different types of data: (i) *Depth images* [29, 30], which include RGB and depth information of images; (ii) *Videos* [31, 32], that is, sequences of annotated frames for HPE with tracking purposes; and (iii) *2D RGB images* [33, 34]. Our method performs HPE with *2D RGB image inputs*, since it is more robust to solve in-the-wild HPE problems [2].
- **Pre-processing techniques** - There are three preprocessing techniques which are common in HPE problems: (i) *Landmark detection* [35]; (ii) *3D modeling* [36]; and (iii) *face detection* [37]. Since our method estimates the pose directly from 2D image intensities instead of using landmarks or 3D models, we apply a *face detection* technique to find the head region.
- **HPE techniques** - The survey of [2] splits 2D RGB HPE techniques in (i) *training* [1, 19, 38] and (ii) *training-free* [39, 40] frameworks. Our method fits as a *training* technique based on convolutional neural networks.

### 2.4. Summary and outline

From the above literature review, we find that the challenge of occlusion in head pose estimation is still scarce. For instance, the system in [16] requires the mouth not to be occluded. The procedure in [17] although addressing occlusions, it only focus on landmark detection and it is not extended for real-time tracking, and while the method in [18] includes pose estimation, it only evaluates yaw angles and displays low accuracy for large yaw values.

Model-based methods rely on the chosen head/face model and are very sensitive to landmark detection and tracking errors. They are also more susceptible both to self-occlusions (extreme poses for example) and object occlusions. Learning-based methods do not require the detection of landmarks and therefore avoid the occlusion problem mentioned above, while outperforming model-based methods.

Consequently, our work follows a learning-based approach based on the framework from [19], but adapted to facial occlusions. Specifically, we introduce a novel latent space regression component to approximate the latent space representation of occluded images to that of non-occluded images. Results show that this aids the model to generalize better to occlusions without deprecating the performance in non-occluded faces. Furthermore, since our approach requires occluded labeled data to train and test the neural network, we also propose a novel procedure to generate synthetic occlusions in existing head pose labeled datasets.

The outline of this paper is as follows: Section 3 describes the synthetic occlusion generation procedure and the utilized head pose datasets; Section 4 outlines our end-to-end learning methodology for HPE under occlusions. In Section 5 we compare our implementation to other SoTA methodologies in three benchmark datasets: The first two, BIWI [30] and AFLW2000 [33], with synthetically occluded and original non-occluded images; and the third, Pandora [41], with real-life, natural occlusions. We perform ablation studies for the hyper-parameters used within our framework, as well as for different occlusions severities. We visualize our model’s latent space representation and compare it to a SoTA. Also, we test our model in the real occlusion case concerning an autonomous feeding robot. Lastly, in Section 6 we make concluding remarks and mention some of the current limitations and future work to further improve our methodology.

### **3. Generating a synthetic occluded dataset**

In this section, we introduce a procedure capable of generating synthetic occlusions in images, and describe the datasets used for the head pose estimation.

#### *3.1. Synthetic occlusion generation procedure*

The generation of synthetic data for training in deep learning frameworks has become ever more common and has been proven to be essential in the



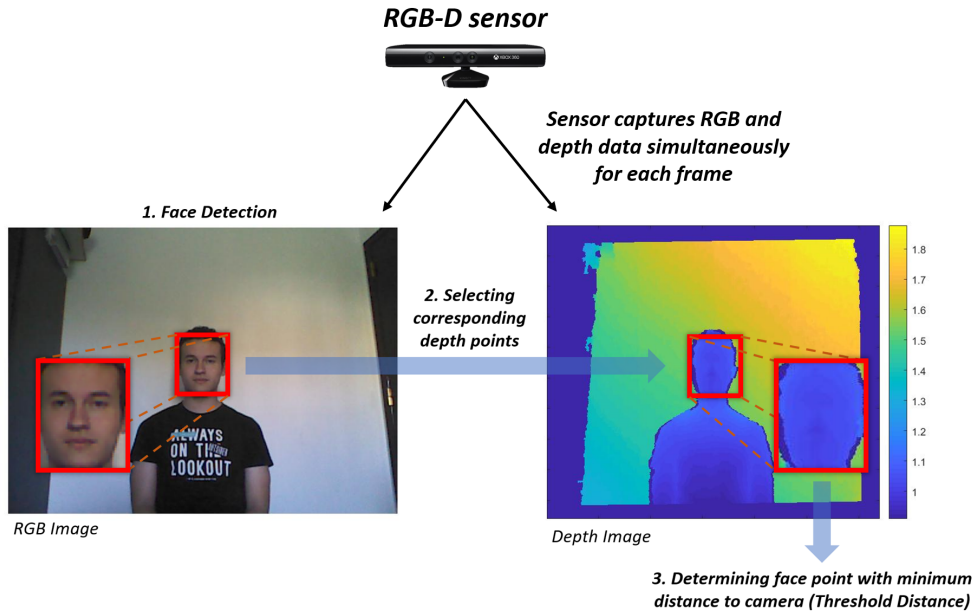
enlargement of training sets and in improving the generalization and accuracy of learning models *e.g.*, medical segmentation [42], autonomous driving [43] and pose estimation [44, 20].

We use existing 2D image head pose datasets that contain thousands of images and respective ground truth pose annotations. However, we intend to train and test our model for occluded images and most datasets contain few or no face occlusions. Thus, we propose a new auxiliary pipeline to generate synthetic occlusions for any RGB image and develop the new occluded datasets required for the training and testing of the deep neural networks implemented in our framework.

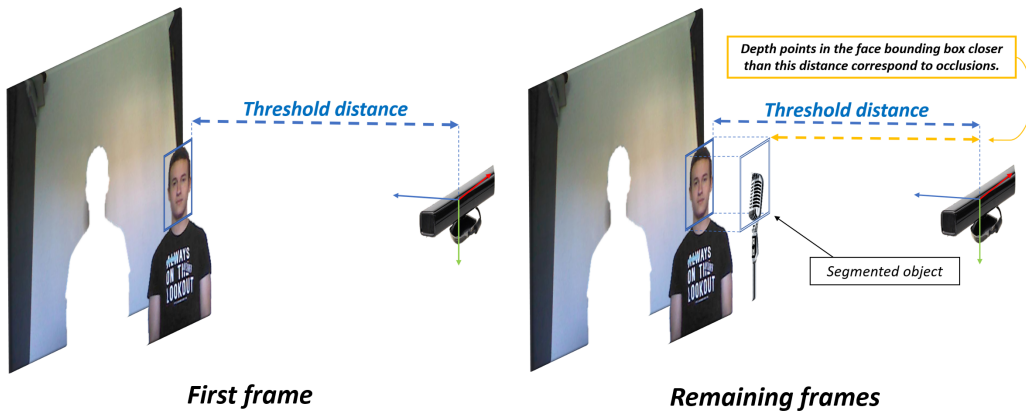
Our procedure to generate synthetic occlusions in images is based on the use of 2D RGB depth data (camera distance to an object). To that end, we use RGB-D cameras which combine RGB and depth sensors and are capable of simultaneously recording the necessary data. We use a Kinect for that purpose. Since such sensors may have inaccuracies, we implement DBSCAN, a density-based clustering algorithm, to remove outliers from the depth data. The procedure, illustrated in Fig. 3, is as follows:

1. Record a in-house video sequence using an RGB-D camera and extract occlusions (Fig. 3 (a)):
  - (a) The first frame must be occlusion free (Fig. 2 (a)). We detect the face in the RGB image, select the corresponding pixels in the depth image and find the one of lowest depth (closest to the camera). This point will correspond to the threshold distance.
  - (b) The remaining frames are occluded. For each one of them we check the depth image for points in the face bounding region at a smaller distance than the threshold depth. Those points belong to occlusion objects (Fig. 2 (b)). We extract the corresponding RGB pixels to obtain and store the segmented occlusion object.
2. When the occlusions from every frame are stored, we re-scale and superimpose the occlusions in the non-occluded face images of benchmark datasets. This way, we generate new occluded labeled datasets. (Fig. 3 (b))

This way, it is straightforward to plug any objects' occlusions in benchmark datasets in a realistic fashion. Instead of superimposing generic synthetic templates on faces, this method allows the generation of any occlusion that appears in specific scenarios/contexts, similar to how they occur in real



(a) 3-step procedure for the first frame



(b) Using threshold distance to extract occlusions

Figure 2: Determining threshold distance for occlusion segmentation (first frame only). The idea is to use the first recorded frame to find the distance between the camera and the face using the 3-step procedure in (a): 1. Apply a face detector to the RGB image of the frame to obtain the face bounding box; 2. Select the depth image points within that bounding box; 3. Determine the minimum distance point to the camera, the threshold distance illustrated in (b). With this, it is possible to determine which pixels in the face region correspond to occlusions that we desire to extract: these points will have a smaller depth when compared to the threshold depth.

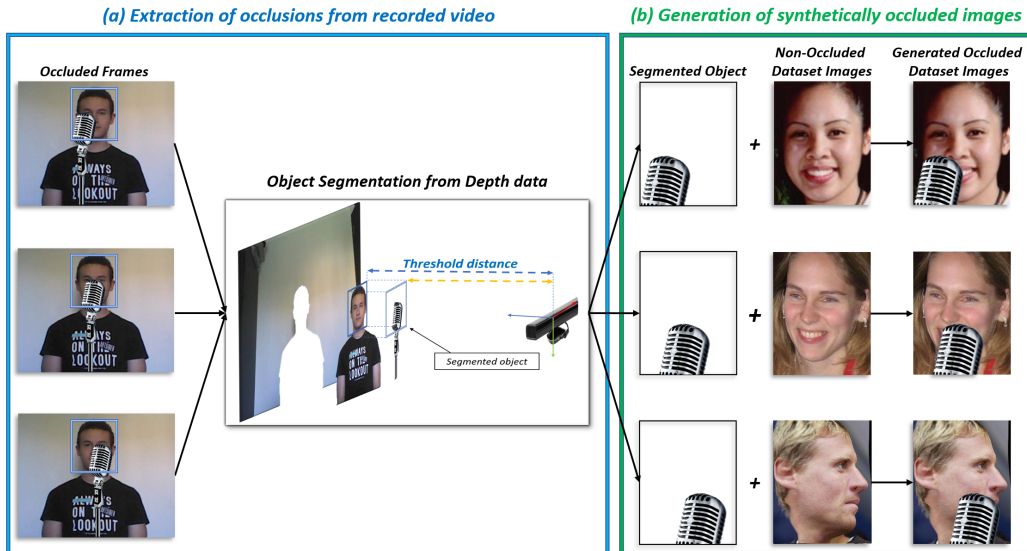


Figure 3: Overall procedure for synthetic occlusion generation in non-occluded images.

life. Notice that this procedure only requires depth data while recording the in-house video sequence and can be applied to any benchmark dataset of RGB images.

### 3.2. Head pose datasets

Following [2], three types of input data can be used: 2D images, depth images and video sequences. We focus on head pose estimation for 2D images, which are ideal for the most challenging in the wild problems. Three head pose datasets are used to apply our procedure and generate new occluded datasets: 300W-LP [33], BIWI [30] and AFLW2000 [33].

The 300W-LP dataset consists of 61,225 face samples and respective vertically flipped versions for a total over 122K examples. It covers a large variation of identity, expression, illumination conditions, pose and it provides facial landmark annotations from which it is possible to extract the pose of the head. It is commonly used in the training process of head pose estimation works [19, 1]. The BIWI dataset contains over 15K images of 20 people and covers about  $\pm 75^\circ$  yaw and  $\pm 60^\circ$  pitch. It is one of the most commonly used benchmarked datasets for HPE challenge. For each frame, it provides a depth image, the corresponding RGB image (both 640x480 pixels), and the ground truth pose annotation. AFLW2000 is a dataset that contains

2K real-world images of diverse head poses which are challenging for face detectors. The pose images include varying lighting and background conditions. This dataset contains annotations for 68 image-level facial landmarks from which the pose can be extracted.

We use occluded versions of the 300W-LP dataset in training and test our methodologies in occluded and non-occluded versions of the BIWI and AFLW2000 datasets.

We also test our method with real-life, natural occlusions from Pandora [41], a dataset for head and shoulder pose, as well as head center localization. Inspired by the automotive context, it simulates driving poses from the point of view of a camera placed inside a dashboard. It contains head and shoulder ground truth pose annotations expressed as yaw, pitch and roll (head pose ranges are  $\pm 70^\circ$  roll,  $\pm 100^\circ$  pitch and  $\pm 125^\circ$  yaw). It includes more than 250K RGB (1920x1080 pixels) and depth images (512x424) with the corresponding annotation. Overall, 10 male and 12 female actors were recorded five times with a Microsoft Kinect One. For testing purposes, we utilize 9619 head occluded images where actors wear garments such as sun glasses, scarves, caps and masks.

#### 4. Methodology for head pose estimation with occlusions

Next, we detail our methodology for the HPE challenge, giving particular attention on how the components of the overall loss are computed.

##### 4.1. End-to-end Multi-loss Approach With Latent Space Regression

Inspired in [19], we propose a new methodology tailored to deal with occlusion as illustrated in Fig. 4. A 2D RGB image is the input of any backbone network. This backbone network is expanded with three extra fully-connected layers which will be used to output the predictions for each Euler angle. The output of the final layer in the backbone network is flattened into a vector which becomes the input for each fully-connected layer. The output of each of the three layers will be a vector of logits. Each vector contains the raw prediction scores (real numbers in range  $[-\infty, +\infty]$ ) for the predicted angle. Each angle in the vector, is represented as a bin that covers a small range in degrees (*e.g.*,  $[0^\circ, 3^\circ]$ ,  $[3^\circ, 6^\circ]$ , ...). The size of these vectors depends on both the angle interval/span for each bin, and the full prediction range for the given Euler angle (*e.g.*, predicting yaw angles in the range  $[-90^\circ, 90^\circ]$ ). Also, in Fig. 4, it can be seen that the output of

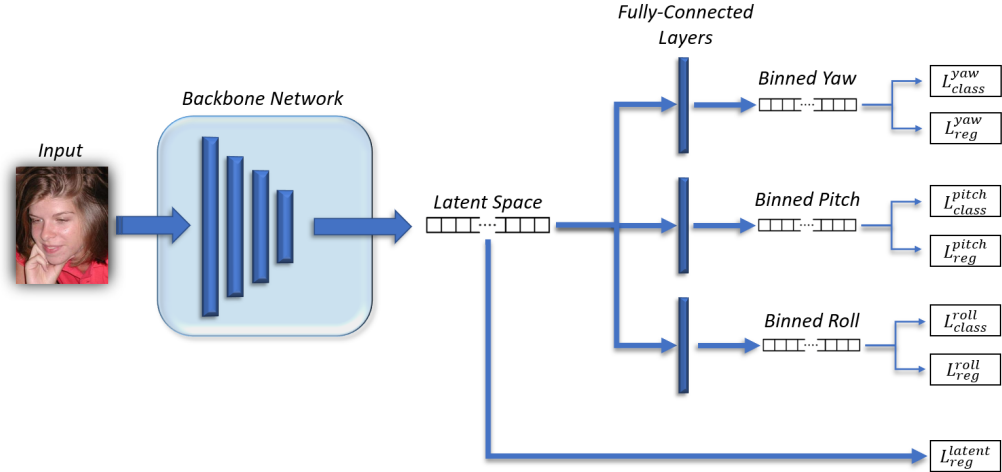


Figure 4: Proposed multi-loss with latent space regression for HPE estimation.

each fully-connected layers is used in a multi-loss scheme that comprises the combination of a classification and regression component to provide an overall loss for a given Euler angle. For the classification task, a softmax activation function plus a cross-entropy loss (also known as categorical cross-entropy loss or softmax loss) is applied to the  $n$ -dimensional vector output of the fully-connected layer. The softmax function converts logits into probabilities by computing the exponents of each bin output and normalizing it by the sum of those exponents so that all probabilities in the activated vector add up to one:

$$S(y_i) = \frac{e^{y_i}}{\sum_{j=1}^n e^{y_j}} \quad (1)$$

where  $y_i$  is the logit for class  $i$ . Afterwards, the cross-entropy loss result is computed by equation (2), where  $t_i$  and  $S(y_i)$  are the ground-truth (0 or 1) and the activation result of the score for each of the  $C$  angle classes/bins, respectively.

$$L_{class} = - \sum_i^C t_i \log(S(y_i)) \quad (2)$$

In addition to the classification loss, the regression component is introduced to determine and regress the error between the predicted angle and

the ground truth in degrees. It is possible to determine the predicted angle in degrees by using the bin probabilities obtained from softmax activation to calculate the expectation of the given angle:

$$\theta_{pred} = w \sum_{i=1}^N p_i \left( i - \frac{1+N}{2} \right) \quad (3)$$

where  $\theta_{pred}$  is the predicted angle in degrees,  $w$  is the width of the bin in degrees,  $N$  is the number of bins for classification, and  $p_i$  is the probability of the angle belonging to bin  $i$ . The offset  $\frac{1+N}{2}$  shifts the bin indices to the respective bin centres, as mentioned in [1]. The loss used for the regression component is the mean squared error (MSE) between the predicted angle  $\theta_{pred}$  and the ground truth angle  $\theta_{gt}$ , for  $N$  predictions.

$$L_{reg} = \frac{1}{N} \sum_{i=1}^N (\theta_{pred} - \theta_{gt})^2 \quad (4)$$

The classification component (2) aims to help the model to predict the vicinity of each pose angle by classifying it in an angle interval bin. The regression component (4) is then introduced to aid the model in achieving fine-grained angle predictions.

The classification and regression loss for the Euler angles are combined using a regularization hyper-parameter  $\alpha$  to manage the trade-off between the two terms. Overall, three losses are used to train the Euler angles:

$$\begin{aligned} L_{yaw} &= L_{class}^{yaw}(y, \hat{y}) + \alpha L_{reg}^{yaw}(y, \hat{y}) \\ L_{pitch} &= L_{class}^{pitch}(y, \hat{y}) + \alpha L_{reg}^{pitch}(y, \hat{y}) \\ L_{roll} &= L_{class}^{roll}(y, \hat{y}) + \alpha L_{reg}^{roll}(y, \hat{y}) \end{aligned} \quad (5)$$

where  $y$  is the predicted value and  $\hat{y}$  is the ground truth for the respective Euler angle loss, provided in the training dataset.

#### 4.1.1. Introducing latent space regression

We introduce a new latent space regression loss, crucial to aid the model to generalize better to occlusions. The latent space, also known as embedding space, is the abstract low-dimensional space that contains the highest-level feature values of the neural network. These values encode the most relevant inner representation of the observed input data and allow to semantically

place similar (pose) outputs closer in the latent space. The idea behind this loss is to approximate the latent space representation of occluded images to that of non-occluded images and therefore allow our model to better predict poses with occlusions. The additional latent space regression loss is the MSE between the predicted latent embedding for occluded images  $E_{pred}$  and the ground truth embedding for non-occluded images  $E_{gt}$ . Thus, for N predictions we have:

$$L_{latent} = \frac{1}{N} \sum_{i=1}^N (E_{pred} - E_{gt})^2 \quad (6)$$

Note that the ground truth latent space embeddings  $E_{gt}$  for non-occluded images is previously extracted from inference on the Hopenet network. The overall loss is the sum of angle and latent losses with a hyper-parameter  $\beta$  to handle the trade-off between them:

$$L = (1 - \beta)(L_{yaw} + L_{pitch} + L_{roll}) + \beta L_{latent} \quad (7)$$

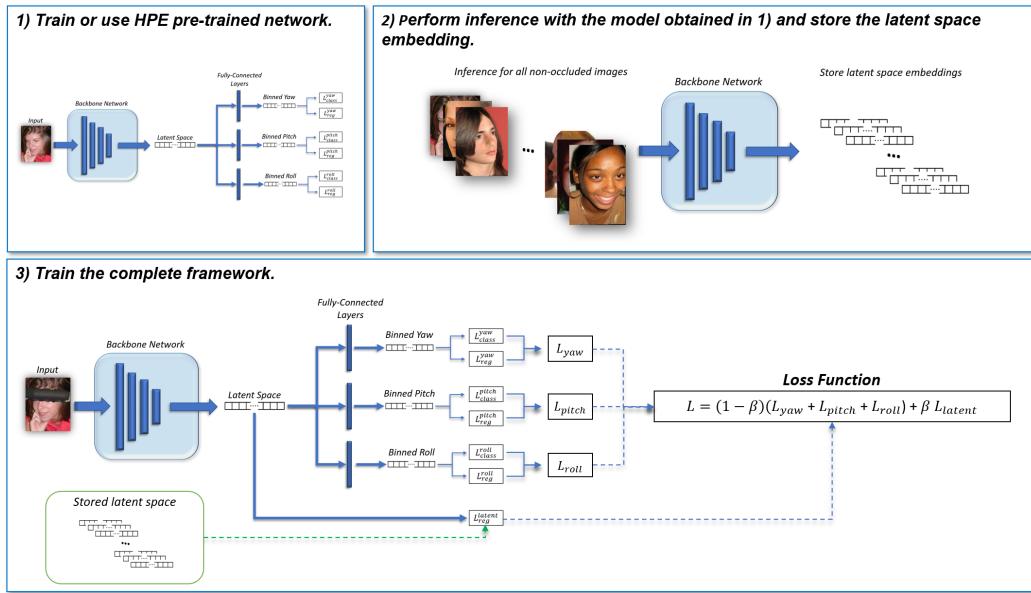


Figure 5: Training procedure representation.

Our complete training procedure is illustrated in Fig. 5 and comprises the following steps:

1. Firstly, we either (i) train or (ii) use a pre-trained model for head pose estimation in non-occluded images. The framework is the same as shown in Fig. 4 apart from the latent space loss;
2. We perform inference with the model obtained in 1), for each non-occluded image and store the flattened output of the final layer in the backbone network. This output corresponds to the representation of the latent space and is used as ground truth for the train with occluded images;
3. Finally, we use the occluded dataset and train the complete framework of Fig. 4, where  $L_{class}^a$  and  $L_{reg}^a$  are the cross-entropy classification loss and MSE regression loss for Euler angle  $a$  (yaw, pitch or roll), and  $L_{reg}^{latent}$  is the MSE regression loss for the latent space.

## 5. Results and discussion

In this section we describe the experiments of the proposed framework. Concretely, we (i) study the impact of varying the hyper-parameters of the framework, (ii) perform a comparison of related SoTA methodologies and (iii) perform an ablation study regarding the severity of the occlusion.

### 5.1. Multi-loss head pose estimation with latent space regression

We evaluate the methodology on both the original and synthetically occluded versions of the BIWI and AFLW2000 datasets as well as with natural occlusions from the Pandora dataset.

We train the framework defined in Section 4.1 using synthetically occluded and non-occluded images of 300W-LP and ResNet-50 as the backbone network. The face images are cropped to the pre-defined input dimension of the ResNet-50 network, 224x224 pixels, and the mean and standard deviation of ImageNet is used to normalize the data. We use 66 bins for classification, each bin has a width of  $3^\circ$ . Our classification vectors cover a range from  $-99^\circ$  to  $99^\circ$  for each Euler angle. There are 31 images of the AFLW2000 dataset that are not used in testing since their pose angles surpass this range.

#### 5.1.1. $\alpha$ -parameter ablation study

We train the framework for 25 epochs with 5 different  $\alpha$  parameter values to determine the best trade off for pose estimation training (see (5)). The head pose estimation error (MAE) results in synthetically occluded and non-occluded datasets are listed in Tables 1 and 2, for the BIWI and AFLW2000



Table 1: Head pose estimation MAE ( $^{\circ}$ ) tests with BIWI for different angle regression weights ( $\alpha$ ).

<i>BIWI</i> [30]	Occluded Images				Combined Average	
$\alpha$	yaw	pitch	roll	Average MAE	$\alpha$	MAE
0.5	5.250	6.529	4.255	5.345	0.5	4.763
1	5.333	6.916	4.036	5.495		
2	5.110	6.832	3.629	<b>5.190</b>		
5	5.477	6.542	4.304	5.441		
10	5.218	7.565	4.344	5.709		
	Non-Occluded Images				2	<b>4.617</b>
0.5	4.259	4.704	3.580	5.441		
1	4.765	4.493	3.956	5.768		
2	4.242	4.041	3.845	4.043		
5	4.474	4.043	3.494	<b>4.004</b>		
10	4.196	4.503	3.628	4.109	10	4.909

datasets, respectively. We can observe that, generally,  $\alpha = 2$  produces the smallest average MAE errors. In particular for occluded images, the lowest MAE errors across all datasets correspond to the networks trained with that parameter value. We can also observe that the largest errors tend to occur for  $\alpha = 1$ . This result highlights the importance of performing this study and selecting the ideal value for this parameter, since  $\alpha = 1$  corresponds to both losses having the same weight. For the following tests, we use  $\alpha = 2$  as the weight for the head pose multi-loss framework.

### 5.1.2. Latent Space Regression Weight Ablation Study

Having determined the best  $\alpha$ , we trained 5 different head pose estimation networks, one for each different value of  $\beta$ . This parameter controls the weight of the latent and angle losses (see (7)). We also perform a comparison between our results and the results of Hopenet [19], WHENet [1], FSA-Net [21], DAD-3D [14], 6DRepNet [25] and Lightweight HPE [26]. We have also considered the model-based method of 3DDFA [15]. However, as argued in [19, 1], this approach is not competitive since on the non-occluded BIWI dataset it provides high values for the estimation error. Our LSR networks are trained for 25 epochs and their parameters are initialized with a pre-trained model provided by the authors of [19] (trained with the origi-

Table 2: Head pose estimation MAE ( $^{\circ}$ ) tests with AFLW2000 for different angle regression weights ( $\alpha$ ).

<i>AFLW2000</i> [33]	Occluded Images				Combined Average	
	yaw	pitch	roll	Average MAE	$\alpha$	MAE
0.5	6.227	8.271	5.713	6.737	0.5	6.089
1	6.411	8.713	6.017	7.047		
2	5.672	8.101	5.783	<b>6.519</b>	1	6.4075
5	6.156	8.279	5.841	6.759		
10	5.4044	8.407	5.923	6.578		
	Non-Occluded Images				2	<b>5.954</b>
0.5	5.281	6.544	4.497	5.441		
1	5.675	6.868	4.760	5.768	5	6.1065
2	4.886	6.636	4.643	<b>5.389</b>		
5	5.403	6.413	4.546	5.454	10	6.0185
10	4.986	6.695	4.696	5.459		

nal 300W-LP dataset). We use the latent space produced by this pre-trained model in non-occluded inference as ground truth in the latent regression loss. To optimize the parameters we use the Adam optimization algorithm with a learning rate of  $10^{-5}$ . We tested our method for all datasets with LSR networks trained on occluded and non-occluded images. For the networks of SoTA methods we utilized the trained models provided by the authors in their official repositories available online on GitHub. The synthetically occluded datasets for training and testing include 25 different recorded occlusions. Tables 3 and 4 display the results for BIWI and AFLW2000 datasets, respectively.

We observe that FSA-NET, Lightweight and WHENet produce the highest yaw error and average MAE in occluded images. A possible explanation for the higher errors in FSA-NET is that this model is based on feature aggregation relying on structural spatial information of the face. This causes the occlusion to affect the predictions. Occlusions also seem to affect the method of image rectification in the Lightweight framework. As for WHENet, the results for occluded images are particularly worse on BIWI. This highlights that this method struggles with occlusions specially in low resolution images. Despite the similarities to Hopenet, WHENet’s training for  $360^{\circ}$  yaw degrees may lead the model to confuse occlusions with more extreme yaw values where the face is also not as visible. As for DAD-3D and 6DRepNet,

Table 3: Head pose estimation MAE ( $^{\circ}$ ) tests with BIWI for different latent space regression weights ( $\beta$ ). LSR stands for latent space regression.

<i>BIWI</i> [30]	Occluded images				Combined Average	
Methods	Yaw	Pitch	Roll	Average MAE	$\beta$	MAE
FSA-Net [21]	10.987	9.848	7.846	9.560	FSA-Net	7.364
WHENet [1]	21.101	13.188	11.225	15.171		
Hopenet [19]	6.725	8.616	7.338	7.560	WHENet	9.822
6DRepNet [25]	7.883	14.983	9.665	10.844		
DAD-3D [14]	5.532	7.924	7.478	6.978	Hopenet	5.661
Lightweight [26]	10.784	9.654	10.309	10.249		
LSR ( $\beta = 0$ )	5.990	7.778	4.346	6.038	6DRepNet	7.252
LSR ( $\beta = 0.5$ )	5.797	7.394	4.537	5.910		
LSR ( $\beta = 0.990$ )	5.798	6.881	4.572	5.750	DAD	5.298
LSR ( $\beta = 0.999$ )	<b>5.174</b>	6.622	4.117	5.304		
LSR ( $\beta = 1$ )	5.429	<b>4.823</b>	<b>3.467</b>	<b>4.573</b>		
	Non-occluded images				Lightweight	7.292
FSA-Net [21]	5.420	5.568	4.515	5.168	0	5.307
WHENet [1]	4.395	4.346	4.674	4.472		
Hopenet [19]	4.375	3.559	3.348	3.761	0.5	5.102
6DRepNet [25]	<b>3.230</b>	4.658	3.091	3.660		
DAD-3D [14]	3.314	4.630	<b>3.090</b>	3.618	0.990	4.925
Lightweight [26]	4.267	5.015	3.722	4.335		
LSR ( $\beta = 0$ )	4.940	4.873	3.911	4.575	0.999	4.669
LSR ( $\beta = 0.5$ )	4.413	4.910	3.556	4.293		
LSR ( $\beta = 0.990$ )	4.204	4.343	3.750	4.099	1	<b>4.046</b>
LSR ( $\beta = 0.999$ )	4.297	4.186	3.617	4.033		
LSR ( $\beta = 1$ )	4.291	<b>3.086</b>	3.179	<b>3.519</b>		

Table 4: Head pose estimation MAE ( $^{\circ}$ ) tests with AFLW2000 for different latent space regression weights ( $\beta$ ). LSR stands for latent space regression.

Methods	Occluded images				Combined Average	
	Yaw	Pitch	Roll	Average MAE	$\beta$	MAE
FSA-Net [21]	13.664	10.880	10.067	11.537	FSA-Net	8.590
WHENet [1]	16.515	11.669	10.267	12.817		
Hopenet [19]	12.438	10.277	8.586	10.434	WHENet	9.028
6DRepNet [25]	8.904	9.799	7.408	8.704		
DAD-3D [14]	7.084	14.953	13.680	11.906	Hopenet	7.579
Lightweight [26]	10.771	9.278	8.335	9.461		
LSR ( $\beta = 0$ )	5.057	7.120	4.961	5.713	6DRepNet	6.181
LSR ( $\beta = 0.5$ )	4.891	6.424	4.918	5.411		
LSR ( $\beta = 0.990$ )	<b>4.714</b>	6.360	4.906	5.327	DAD-3D	7.762
LSR ( $\beta = 0.999$ )	4.741	6.254	4.765	<b>5.253</b>		
LSR ( $\beta = 1$ )	5.117	<b>6.075</b>	<b>4.590</b>	5.261		
Non-occluded images						
FSA-Net [21]	5.109	6.462	3.356	5.642	Lightweight	6.898
WHENet [1]	4.475	6.222	5.017	5.238	0	5.220
Hopenet [19]	4.965	5.250	3.956	4.724		
6DRepNet [25]	3.230	4.658	3.091	3.659	0.5	4.914
DAD-3D [14]	<b>3.134</b>	<b>4.630</b>	<b>3.090</b>	<b>3.618</b>		
Lightweight [26]	4.267	5.015	3.722	4.335	0.990	4.882
LSR ( $\beta = 0$ )	4.114	6.002	4.061	4.726		
LSR ( $\beta = 0.5$ )	3.855	5.447	3.947	4.416	0.999	<b>4.833</b>
LSR ( $\beta = 0.990$ )	3.709	5.517	4.083	4.436		
LSR ( $\beta = 0.999$ )	3.813	5.420	4.003	4.412	1	4.867
LSR ( $\beta = 1$ )	4.258	5.272	3.888	4.473		

they present the lowest non-occluded estimation errors, but pitch and roll estimations are heavily affected by occlusions.

When we do not consider the latent space regression ( $\beta = 0$ ), similar to [19], the error for occluded images decreases but the performance for non-occluded images deteriorates significantly. This is more evident on the BIWI dataset, where the average MAE for non-occluded images increases by nearly  $1^\circ$ . We can also observe that as the  $\beta$  parameter increases, the MAE becomes lower for both occluded images and non-occluded images. On AFLW2000 the non-occluded estimation results improve on the Hopenet scores. This confirms that introducing the latent regression loss (see (7)) helps not only to achieve improved generalization for occlusions, but also to avoid detouring from accurate non-occluded pose estimation. While for  $\beta = 1$  the average MAE errors are the best on BIWI, we verify that this parameter leads to a worse estimation of yaw values, which is the most varied and relevant Euler angle in head pose estimation. From the above,  $\beta = 0.999$  provides the best trade-off for the MAE and yaw estimation.

Table 5: Head pose estimation MAE ( $^\circ$ ) tests with Pandora for different latent space regression weights ( $\beta$ ). LSR stands for latent space regression.

<i>Pandora</i> [41]				
Methods	Yaw	Pitch	Roll	Average MAE
FSA-Net [21]	11.736	8.607	6.691	9.011
WHENet [1]	11.352	6.281	6.453	8.029
Hopenet [19]	10.442	7.239	6.925	8.202
6DRepNet [25]	10.896	6.897	7.500	8.431
DAD-3D [14]	9.348	7.437	8.474	8.420
Lightweight [26]	10.133	8.690	7.064	8.629
LSR ( $\beta = 0$ )	9.178	6.296	6.895	7.456
LSR ( $\beta = 0.5$ )	9.135	5.968	6.665	7.256
LSR ( $\beta = 0.990$ )	<b>9.084</b>	5.690	6.565	7.113
LSR ( $\beta = 0.999$ )	9.096	<b>5.657</b>	<b>6.215</b>	<b>6.989</b>
LSR ( $\beta = 1$ )	9.60596	5.820	6.368	7.265

Overall, our lowest average MAE model on BIWI is able to decrease the error for occluded images in approximately  $2.4^\circ$ , when compared to the

best SoTA result (DAD-3D). As for AFLW, our model decreases the error in nearly  $3.5^\circ$  in comparison to the best SoTA result (6DRepNet).

Table 5 display the results for naturally occluded images of the Pandora dataset. FSA-Net and WHENet produce the highest yaw estimation errors. The Lightweight network once more is one of the most affected by occlusions, with the second highest average MAE. DAD-3D presents the lowest yaw estimation from SoTA methods, but one of the highest regarding pitch and roll. Our model also exhibit the lowest errors for this dataset with  $\beta = 0.990$  presenting the lowest yaw error and  $\beta = 0.999$  the lowest average MAE. The error decreased in  $1.04^\circ$  when compared to the best SoTA result (WHENet).

### 5.2. Ablation study for several occlusion severities

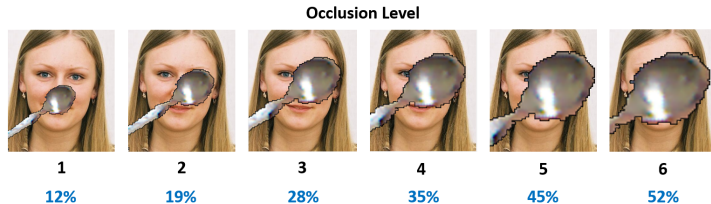


Figure 6: Occlusion severity levels.

Table 6: Average MAE ( $^\circ$ ) comparison for occlusion dimension levels.

Datasets	Methods \ Occlusion level	1	2	3	4	5	6
BIWI [30]	Hopenet [19]	5.409	6.299	7.633	9.329	11.178	13.168
	Latent (LSR)	4.755	5.201	5.646	6.503	8.130	10.108
AFLW2000 [33]	Hopenet [19]	6.982	8.933	11.231	12.945	14.474	15.317
	Latent (LSR)	5.783	6.113	6.686	7.341	8.545	9.377

In order to evaluate the robustness of our method against the occlusions, we performed an ablation study for different occlusion levels. To accomplish this, we simulated a feeding scenario. Concretely, we recorded an object, a spoon, in eleven different positions and orientations. This object is introduced in the images of both AFLW2000 and BIWI datasets, resulting in occluded versions of these two datasets. For this purpose, we applied our synthetic occlusion generation procedure (see Sec. 3) and gradually augment the size of the spoon occlusions.

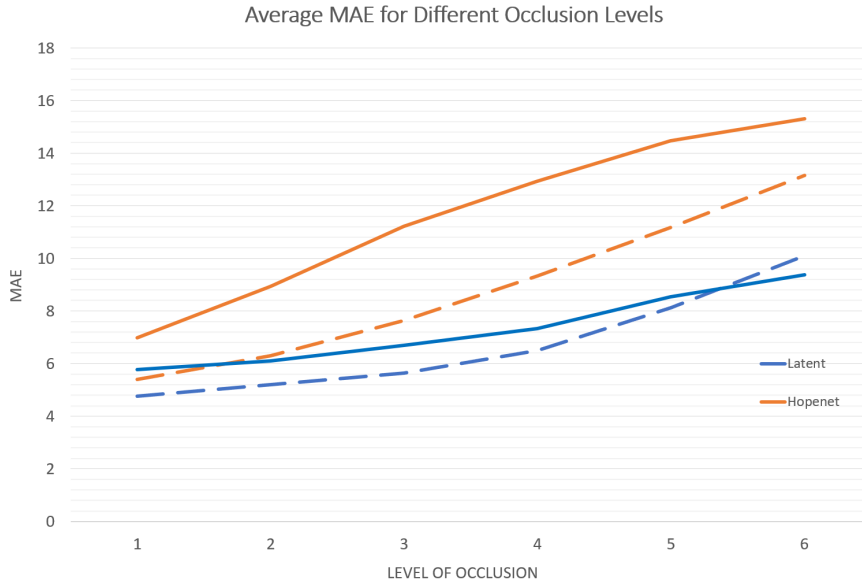


Figure 7: Average MAE comparison for occlusion dimension levels. Solid and dashed lines correspond to AFLW2000 and BIWI results, respectively.

We defined six levels of occlusions, ranging from one (lowest occlusion level) to six (highest occlusion level). As such, we generated six different occluded datasets for each AFLW2000 and BIWI datasets (twelve datasets are thus used in this experiment). Examples from occlusion severity levels and respective average occlusion percentages for each dataset can be seen in Fig. 6. The percentages are computed as the proportion of pixels in the original dataset face images that become occluded. We perform a comparison between the proposed methodology and Hopenet, as we next describe. The results depicted in Fig. 7 show that the difference in the estimation error between our model and Hopenet increases as we augment the occlusion (until level four). For the largest occlusions (level six) our model decreases the average estimation error in 39% on AFLW2000 and 23% on BIWI. Not only does it perform better with occlusions but it is also more robust to occlusion severity variations. The difference in the average MAE between levels one and six is around  $8^\circ$  for Hopenet in both datasets, while for our model it is around  $5^\circ$  on BIWI and lower than  $4^\circ$  on AFLW2000. Furthermore, our model’s error estimation for level six on AFLW2000 is lower than *Hopenet*’s error for level three occlusions and only slightly higher than level two. These

results confirm that our model significantly improves the robustness of the estimation, even for very large occlusions.

### 5.3. *t*-SNE latent space visualization

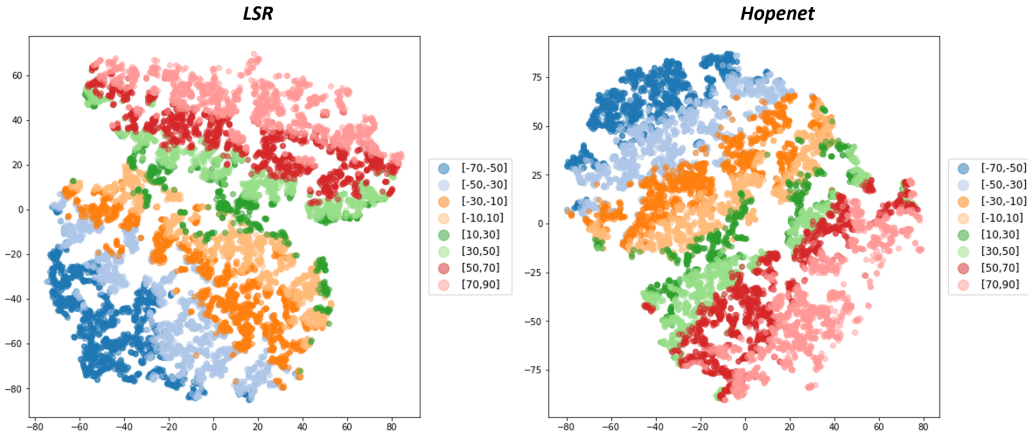


Figure 8: *t*-SNE latent space visualization - non-occluded images. Data points from similar poses closer to each other and dissimilar poses far apart. - good data arrangement.

The latent space is an abstract multi-dimensional space that maps a relevant internal representation of how a neural network interprets external input data and provides insight on what learned from training. In this space, the distance of data points is related to the semantic similarity of the input data. As such, similar items are closer to one another in this space, while dissimilar items are further apart. We performed inference in non-occluded and occluded face images using both our model and Hopenet. The output latent embeddings were stored in order to apply the *t*-Distributed Stochastic Neighbor Embedding (*t*-SNE) technique. This is a non-linear method that allows to visualize high-dimensional data by giving each datapoint a location in a two or three-dimensional map. In short, it is a visualization technique. The idea is to gain an intuition of how the models interpret and arrange both non-occluded and occluded data. In this space, a good HPE model should exhibit images of similar pose angles closer to each another and images of dissimilar poses further apart, with and without occlusions.

The resultant *t*-SNE 2D maps can be seen in Figs. 8, 9 for non-occluded and occluded images, respectively.



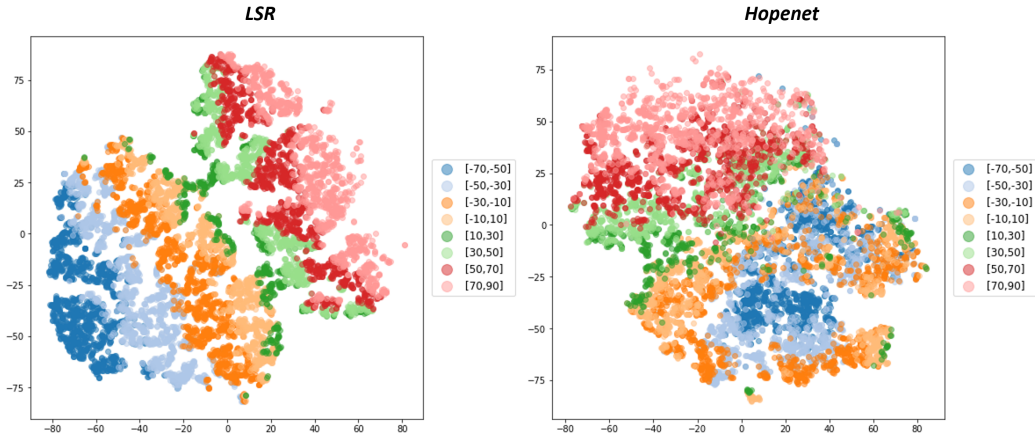


Figure 9: t-SNE latent space visualization - occluded images. Data points of different pose angles mixed for Hopenet. However, our model displays data points arranged in a continuous manner as it did for non-occluded images.

The t-SNE visualization for non-occluded images (see Fig. 8) displays a good data arrangement for both models, since the data points in the latent space are arranged from the lowest values of pose angles to the highest (and vice-versa) in a continuous progressive manner. Similar pose angles are next to each other (e.g. angles in  $[-70^\circ, -50^\circ[$  next to  $[-50^\circ, -30^\circ[$ , which in turn are next to  $[-30^\circ, -10^\circ[$ ) and dissimilar are further apart (e.g. the most distant points from the  $[-70^\circ, -50^\circ[$  range are in the  $[70^\circ, 90^\circ[$  range).

The t-SNE visualization for occluded images of Hopenet (see Fig. 9) displays a much more erratic and ambiguous blend of image data points from different angles in several regions of the latent space. For instance, points in the lowest negative range ( $[-70^\circ, -50^\circ[$ ) are now much closer to points in positive ranges (even to the most dissimilar and highest positive range,  $[70^\circ, 90^\circ[$ ) and very mixed with all negative ranges. In contrast, our model displays significantly better data arrangement for occlusions by presenting a continuous progression of angle values in the latent space, as it did for non-occluded images. These t-SNE representations therefore provide an intuitive visual insight on how Hopenet struggles in distinguishing between different poses with occluded image inputs, while our model, aided by latent space regression, exhibits a good semantic understanding of head poses regardless of the face being occluded or not.

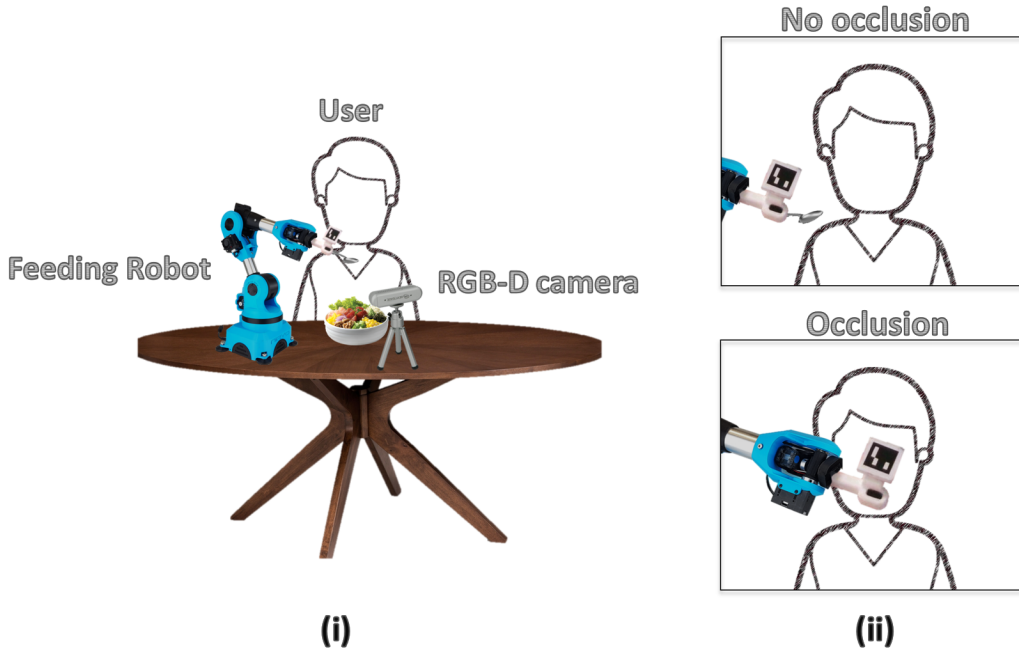


Figure 10: Feedbot’s framework in autonomous feeding scenario (i) and camera point of view (ii).

#### 5.4. A real case: the feeding robot scenario

We tested our best method in the feeding context of Feedbot [45], an autonomous feeding robot designed for people with upper-extremity disabilities. The Feedbot framework, illustrated in Fig. 10 (i), includes a RGB-D camera and a modular robotic arm to perform assisted feeding. The robotic arm is set close to the user to be able to perform the feeding task and the camera is placed in front of the user, but more distant. This way, the camera captures the entire environment, including the user and the robotic arm, as shown in Fig. 10 (ii). The end-effector of the robotic arm has a spoon to collect the food from the plate and a RGB camera that provides visual feedback on whether it was captured to improve food acquisition efficiency. A point cloud registration algorithm is implemented to use the 3D data captured by the RGB-D sensor and a 3D face model to compute rigid head transformations and track the head pose and mouth of the user. This tracking allows the food to be effectively brought to the user’s mouth, rather than to a pre-defined feeding location. However, the robotic arm occludes the face while feeding, which makes the head pose estimation and tracking much more diffi-

## Non-occluded frames

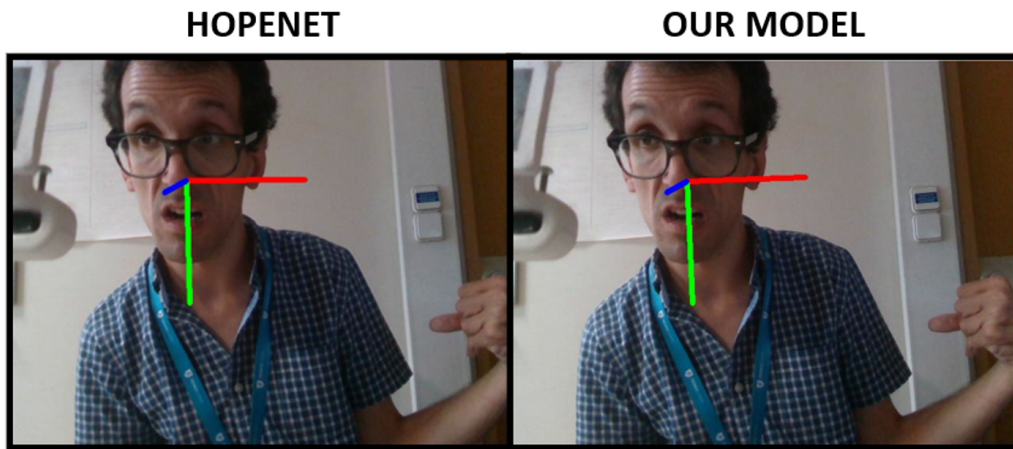


Figure 11: Feedbot scenario: Comparison between Hopenet and our model. HPE is good and similar for both models in non-occluded frames.

cult. We recorded a video where Feedbot’s robotic arm executes the feeding task and occludes the face of the user. We performed inference for the entire video using both our and *Hopenet*’s models, which exhibited the lowest error among the tested SoTA models in Section 5.1.2. Since we do not have the ground truth pose in this testing conditions, we carry out a qualitative analysis and evaluation in this section.

Initially, when the robot is not yet feeding the user, the head is not occluded by the robotic arm and our model’s pose estimation is accurate and identical to that of SoTA Hopenet, as seen in Fig. 11. This is the desired behaviour since we intend to improve on occluded head pose estimation, while preserving the SoTA accuracy for non-occluded images.

When the robot moves the spoon towards the user’s mouth, it occludes the face with the end-effector. Fig. 12 displays a set of occluded frames which show clear improvements in the head pose estimation of our model when compared to Hopenet. In these examples, Hopenet estimates head poses in opposite direction to that of which the head is turned. These results outline the difficulties that model has with the occlusions generated by the robot. Contrasting with the above, we verify that our model is noticeably more robust to this problem and estimates the head poses much closer to

## Occluded frames

HOPENET

OUR MODEL

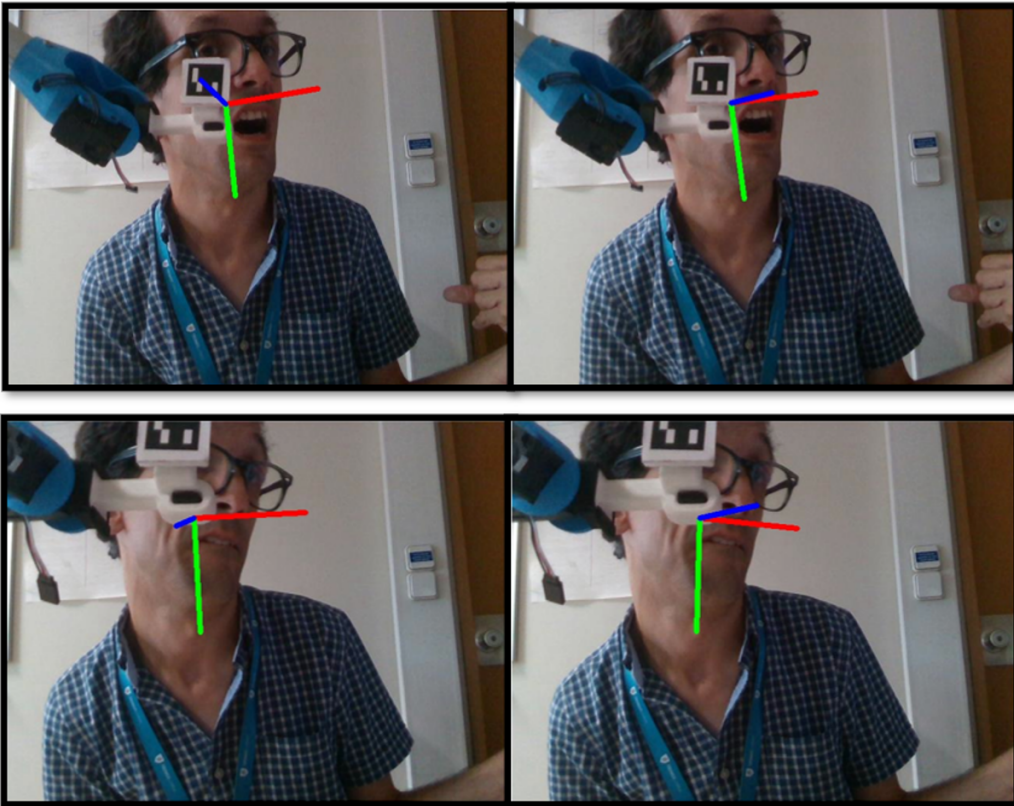


Figure 12: Feedbot scenario: Comparison between Hopenet and our model. For occluded frames, however, Hopenet does not estimate the pose correctly. Our model correctly estimates the pose, despite the occlusions.

reality despite the partial occlusions, particularly improving the yaw rotation around the green axis (the most important pose rotation) when compared to Hopenet.

## 6. Conclusion

In this work, we developed a learning-based methodology to deal with the occlusion problem in head pose estimation. To be able to implement and test this approach, we introduced an auxiliary procedure to generate synthetic occlusions in face images using an RGB-D camera. We show how to segment occlusions based on depth data captured by the camera and how to inpaint the occlusion in any RGB face image. We applied this procedure to three datasets and generated synthetically occluded versions for each dataset.

We designed a new multi-loss head pose estimation framework combined with a latent space regression loss. We showed that introducing such latent space regression term in the loss is fundamental for the accuracy improvement and generalization for occluded images and non-occluded images. We performed an ablation study varying the occlusion severity and demonstrated that our model is far more robust to large occlusions when compared with Hopenet. We visualized the latent space representation using the t-SNE technique. We verified that the latent regression component in training allowed our model to achieve good data arrangement in regard to pose angles for non-occluded and occluded images particularly, which translated in better pose estimation.

We carried out qualitative tests in the real world application of the Feedbot, an autonomous assisting feeding robot. Our model improved the head pose estimation for the occlusions of the robotic arm when compared to a SoTA estimation model, while achieving identical performance without occlusions.

### 6.1. Method limitations and future work

Despite achieving good results, the developed methodologies have some limitations and further work could be done to improve them.

The RGB camera of the Microsoft Kinect has low image resolution (640x480 pixels), which leads to synthetic occlusions of low definition. To improve the occluded datasets, an RGB-D sensor of higher resolution could be used to generate better defined synthetic occlusions.

The convolutional neural network we used in pose estimation frameworks, ResNet-50, is a large network with over 23 million parameters and is therefore slower to train and requires more GPU power. A lighter network such as EfficientNet [46], with 11 million parameters, could be used to address this issue and allow implementations in low-cost hardware.

A method regarding the reconstruction of occluded faces could also be a good strategy to this problem. Particularly, a Generative Adversarial Network could be explored for the face generation.

## References

- [1] Y. Zhou, J. Gregson, Whenet: Real-time fine-grained estimation for wide range head pose (2020). [arXiv:2005.10353](https://arxiv.org/abs/2005.10353).
- [2] A. Abate, C. Bisogni, A. Castiglione, M. Nappi, Head pose estimation: An extensive survey on recent techniques and applications, *Pattern Recognition* 127 (2022) 108591. [doi:10.1016/j.patcog.2022.108591](https://doi.org/10.1016/j.patcog.2022.108591).
- [3] A. Fernández, R. Usamentiaga, J. L. Carús, R. Casado, Driver distraction using visual-based sensors and algorithms, *Sensors* 16 (11) (2016). [doi:10.3390/s16111805](https://doi.org/10.3390/s16111805).
- [4] S. J. Ray, J. Teizer, Coarse head pose estimation of construction equipment operators to formulate dynamic blind spots, *Adv. Eng. Inform.* 26 (1) (2012) 117–130. [doi:10.1016/j.aei.2011.09.005](https://doi.org/10.1016/j.aei.2011.09.005).
- [5] M. C. d. F. Macedo, A. L. Apolinário, A. C. d. S. Souza, A robust real-time face tracking using head pose estimation for a markerless ar system, in: *2013 XV Symposium on Virtual and Augmented Reality*, 2013, pp. 224–227. [doi:10.1109/SVR.2013.12](https://doi.org/10.1109/SVR.2013.12).
- [6] F. Nihei, Y. I. Nakano, Exploring methods for predicting important utterances contributing to meeting summarization, *Multimodal Technologies and Interaction* 3 (2019) 50. [doi:10.3390/mti3030050](https://doi.org/10.3390/mti3030050).
- [7] I. Reid, B. Benfold, A. Patron-Perez, E. Sommerlade, Understanding interactions and guiding visual surveillance by tracking attention, *Vol. 6468*, 2010, pp. 380–389. [doi:10.1007/978-3-642-22822-3\textunderscore38](https://doi.org/10.1007/978-3-642-22822-3_textunderscore38).

- [8] C.-W. Chen, H. Aghajan, Multiview social behavior analysis in work environments, 2011, pp. 1 – 6. doi:10.1109/ICDSC.2011.6042910.
- [9] K. Sankaranarayanan, M.-C. Chang, N. Krahnstoeber, Tracking gaze direction from far-field surveillance cameras, in: 2011 IEEE Workshop on Applications of Computer Vision (WACV), 2011, pp. 519–526. doi:10.1109/WACV.2011.5711548.
- [10] K. Smith, S. O. Ba, J.-M. Odobez, D. Gatica-Perez, Tracking the visual focus of attention for a varying number of wandering people, *IEEE Transactions on Pattern Analysis and Machine Intelligence* 30 (7) (2008) 1212–1229. doi:10.1109/TPAMI.2007.70773.
- [11] T. Hassner, S. Harel, E. Paz, R. Enbar, Effective face frontalization in unconstrained images (11 2014). doi:10.1109/CVPR.2015.7299058.
- [12] J. M. Diaz Barros, B. Mirbach, F. Garcia, K. Varanasi, D. Stricker, Real-Time Head Pose Estimation by Tracking and Detection of Key-points and Facial Landmarks, 2019, pp. 326–349. doi:10.1007/978-3-030-26756-8\textunderscore16.
- [13] H. Yuan, M. Li, J. Hou, J. Xiao, Single image-based head pose estimation with spherical parametrization and 3d morphing, *Pattern Recognition* 103 (2020) 107316. doi:10.1016/j.patcog.2020.107316.
- [14] T. Martyniuk, O. Kupyn, Y. Kurlyak, I. Krashenyi, J. Matas, V. Sharmanska, Dad-3dheads: A large-scale dense, accurate and diverse dataset for 3d head alignment from a single image, in: *Proc. IEEE Conf. on Computer Vision and Pattern Recognition (CVPR)*, 2022.
- [15] J. Guo, X. Zhu, Y. Yang, F. Yang, Z. Lei, S. Z. Li, Towards fast, accurate and stable 3d dense face alignment, in: A. Vedaldi, H. Bischof, T. Brox, J.-M. Frahm (Eds.), *Computer Vision – ECCV 2020*, Springer International Publishing, Cham, 2020, pp. 152–168.
- [16] M. Wenzel, W. Schiffmann, Head pose estimation of partially occluded faces, 2005, pp. 353– 360. doi:10.1109/CRV.2005.45.
- [17] Y. Wu, Q. Ji, Robust facial landmark detection under significant head poses and occlusion, 2015 *IEEE International Conference on Computer Vision (ICCV)* (2015) 3658–3666.

- [18] Y. Wu, C. Gou, Q. Ji, Simultaneous facial landmark detection, pose and deformation estimation under facial occlusion, 2017 IEEE Conference on Computer Vision and Pattern Recognition (CVPR) (2017) 5719–5728.
- [19] N. Ruiz, E. Chong, J. M. Rehg, Fine-grained head pose estimation without keypoints, 2018 IEEE/CVF Conference on Computer Vision and Pattern Recognition Workshops (CVPRW) (2018) 2155–215509.
- [20] Y. Xu, C. Jung, Y. Chang, Head pose estimation using deep neural networks and 3d point cloud, Pattern Recognition 121 (2021) 108210. doi:10.1016/j.patcog.2021.108210.
- [21] T.-Y. Yang, Y.-T. Chen, Y.-Y. Lin, Y.-Y. Chuang, Fsa-net: Learning fine-grained structure aggregation for head pose estimation from a single image, in: 2019 IEEE/CVF Conference on Computer Vision and Pattern Recognition (CVPR), 2019, pp. 1087–1096. doi:10.1109/CVPR.2019.00118.
- [22] T.-Y. Yang, Y.-H. Huang, Y.-Y. Lin, P.-C. Hsiu, Y.-Y. Chuang, Ssr-net: A compact soft stagewise regression network for age estimation, in: Proceedings of the Twenty-Seventh International Joint Conference on Artificial Intelligence, IJCAI-18, International Joint Conferences on Artificial Intelligence Organization, 2018, pp. 1078–1084. doi:10.24963/ijcai.2018/150.
- [23] V. Albiero, X. Chen, X. Yin, G. Pang, T. Hassner, img2pose: Face alignment and detection via 6dof, face pose estimation, 2021 IEEE/CVF Conference on Computer Vision and Pattern Recognition (CVPR) (2021) 7613–7623.
- [24] H.-W. Hsu, T.-Y. Wu, S. Wan, W. H. Wong, C.-Y. Lee, Quatnet: Quaternion-based head pose estimation with multiregression loss, IEEE Transactions on Multimedia 21 (4) (2019) 1035–1046. doi:10.1109/TMM.2018.2866770.
- [25] T. Hempel, A. A. Abdelrahman, A. Al-Hamadi, 6d rotation representation for unconstrained head pose estimation, in: 2022 IEEE International Conference on Image Processing (ICIP), 2022, pp. 2496–2500. doi:10.1109/ICIP46576.2022.9897219.



- [26] X. Li, D. Zhang, M. Li, D.-J. Lee, Accurate head pose estimation using image rectification and a lightweight convolutional neural network, *IEEE Transactions on Multimedia* (2022) 1–1doi:10.1109/TMM.2022.3144893.
- [27] H.-W. Hsu, T.-Y. Wu, S. Wan, W. H. Wong, C.-Y. Lee, Quatnet: Quaternion-based head pose estimation with multiregression loss, *IEEE Transactions on Multimedia* 21 (4) (2019) 1035–1046. doi:10.1109/TMM.2018.2866770.
- [28] Y. Wang, G. Yuan, X. Fu, Driver’s head pose and gaze zone estimation based on multi-zone templates registration and multi-frame point cloud fusion, *Sensors* 22 (2022) 3154. doi:10.3390/s22093154.
- [29] T. Baltrušaitis, P. Robinson, L.-P. Morency, 3d constrained local model for rigid and non-rigid facial tracking, *2012 IEEE Conference on Computer Vision and Pattern Recognition* (2012) 2610–2617.
- [30] K. S. Mader, *Biwi Kinect Head Pose Database* (2018).
- [31] M. Ariz, J. J. Bengoechea, A. Villanueva, R. Cabeza, A novel 2d/3d database with automatic face annotation for head tracking and pose estimation., *Comput. Vis. Image Underst.* 148 (2016) 201–210.
- [32] M. La Cascia, S. Sclaroff, V. Athitsos, Fast, reliable head tracking under varying illumination: an approach based on registration of texture-mapped 3d models, *IEEE Transactions on Pattern Analysis and Machine Intelligence* 22 (4) (2000) 322–336. doi:10.1109/34.845375.
- [33] X. Zhu, X. Liu, Z. Lei, S. Z. Li, Face alignment in full pose range: A 3d total solution, *IEEE Transactions on Pattern Analysis and Machine Intelligence* 41 (1) (2019) 78–92. doi:10.1109/tpami.2017.2778152.
- [34] X. Yin, X. Yu, K. Sohn, X. Liu, M. Chandraker, Towards large-pose face frontalization in the wild, *2017 IEEE International Conference on Computer Vision (ICCV)* (2017) 4010–4019.
- [35] S. Colaco, D. S. Han, Facial keypoint detection with convolutional neural networks, in: *2020 International Conference on Artificial Intelligence in Information and Communication (ICAIIIC)*, 2020, pp. 671–674. doi:10.1109/ICAIIIC48513.2020.9065279.

- [36] H. Proença, J. Neves, T. Marques, S. Barra, J. Moreno, Joint head pose / soft label estimation for human recognition in-the-wild, *IEEE Transactions on Pattern Analysis and Machine Intelligence* 38 (2016) 1–1. doi:10.1109/TPAMI.2016.2522441.
- [37] J. Deng, J. Guo, N. Xue, S. Zafeiriou, Arcface: Additive angular margin loss for deep face recognition, in: 2019 IEEE/CVF Conference on Computer Vision and Pattern Recognition (CVPR), 2019, pp. 4685–4694. doi:10.1109/CVPR.2019.00482.
- [38] K. Chen, K. Jia, H. Huttunen, J. Matas, J.-K. Kämäräinen, Cumulative attribute space regression for head pose estimation and color constancy, *Pattern Recognition* 87 (10 2018). doi:10.1016/j.patcog.2018.10.015.
- [39] P. Barra, C. Bisogni, M. Nappi, S. Ricciardi, Fast QuadTree-Based Pose Estimation for Security Applications Using Face Biometrics: 12th International Conference, NSS 2018, Hong Kong, China, August 27-29, 2018, Proceedings, 2018, pp. 160–173. doi:10.1007/978-3-030-02744-5\textunderscore12.
- [40] A. F. Abate, P. Barra, C. Bisogni, M. Nappi, S. Ricciardi, Near real-time three axis head pose estimation without training, *IEEE Access* 7 (2019) 64256–64265.
- [41] G. Borghi, M. Venturelli, R. Vezzani, R. Cucchiara, Poseidon: Face-from-depth for driver pose estimation, in: 2017 IEEE Conference on Computer Vision and Pattern Recognition (CVPR), IEEE, 2017, pp. 5494–5503.
- [42] I. Khanfir, S. Almouahed, B. Solaiman, E. Bossé, An iterative possibilistic knowledge diffusion approach for blind medical image segmentation, *Pattern Recognition* 78 (06 2018). doi:10.1016/j.patcog.2018.01.024.
- [43] G. Ros, L. Sellart, J. Materzynska, D. Vazquez, A. M. Lopez, The synthia dataset: A large collection of synthetic images for semantic segmentation of urban scenes, in: 2016 IEEE Conference on Computer Vision and Pattern Recognition (CVPR), 2016, pp. 3234–3243. doi:10.1109/CVPR.2016.352.

- [44] Y. Wang, W. Liang, J. Shen, Y. Jia, L.-F. Yu, A deep coarse-to-fine network for head pose estimation from synthetic data, *Pattern Recognition* 94 (05 2019). doi:10.1016/j.patcog.2019.05.026.
- [45] A. Candeias, T. Rhodes, M. Marques, J. a. P. ao Costeira, M. Veloso, Vision augmented robot feeding, in: *Proceedings of the European Conference on Computer Vision (ECCV) Workshops*, 2018.
- [46] M. Tan, Q. Le, EfficientNet: Rethinking model scaling for convolutional neural networks, in: K. Chaudhuri, R. Salakhutdinov (Eds.), *Proceedings of the 36th International Conference on Machine Learning*, Vol. 97 of *Proceedings of Machine Learning Research*, PMLR, 2019, pp. 6105–6114, <https://proceedings.mlr.press/v97/tan19a.html>.